Physics in Medicine & Biology

PAPER • **OPEN ACCESS**

Human lung virtual histology by multi-scale x-ray phase-contrast computed tomography

To cite this article: Jakob Reichmann *et al* 2023 *Phys. Med. Biol.* **68** 115014

IOP Publishing Phys. Med. Biol. 68 (2023) 115014 https://doi.org/10.1088/1361-6560/acd48d

Physics in Medicine & Biology

IPEM Institute of Physics and Engineering in Medicine

OPEN ACCESS

RECEIVED
6 February 2023

REVISED
3 May 2023

ACCEPTED FOR PUBLICATION
11 May 2023

PUBLISHED
30 May 2023

PAPER

Human lung virtual histology by multi-scale x-ray phase-contrast computed tomography

Jakob Reichmann[1], Stijn E Verleden[2], Mark Kühnel[3,4], Jan C Kamp[4,5], Christopher Werlein[3,4], Lavinia Neubert[3,4], Jan-Hendrik Müller[1], Thanh Quynh Bui[1], Maximilian Ackermann[6], Danny Jonigk[4,7] and Tim Salditt[1]

[1] Institute for X-ray Physics, University of Göttingen, Friedrich-Hund-Platz 1, D-37077 Göttingen, Germany
[2] Antwerp Surgical Training, Anatomy and Research Centre (ASTARC), University of Antwerp, Universiteitsplein 1, B-2610 Wilrijk, Belgium
[3] Institute of Pathology, Hannover Medical School, Carl-Neuberg-Str. 1, D-30625 Hannover, Germany
[4] Biomedical Research in Endstage and Obstructive Lung Disease Hannover, German Center for Lung Research, Carl-Neuberg-Str. 1, D-30625 Hannover, Germany
[5] Department of Respiratory Medicine, Hannover Medical School, Carl-Neuberg-Str. 1, D-30625 Hannover, Germany
[6] Institute of Pathology and Department of Molecular Pathology, Helios University Clinic Wuppertal, University of Witten/Herdecke, Heusnerstraße 40, D-42283 Wuppertal, Germany
[7] Institute of Pathology, RWTH Aachen Medical Faculty, Pauwelsstraße 30, D-52074 Aachen, Germany

E-mail: tsaldit@gwdg.de

Keywords: computed tomography, virtual histology, x-ray imaging, phase contrast, human lung, tissue imaging, multiscale

Supplementary material for this article is available online

Abstract

Objectives. As the central organ of the respiratory system, the human lung is responsible for supplying oxygen to the blood, which reaches the erythrocytes by diffusion through the alveolar walls and is then distributed throughout the body. By exploiting the difference in electron density detected by a phase shift in soft tissue, high-resolution x-ray phase-contrast computed tomography (XPCT) can resolve biological structures in a sub-μm range, shedding new light on the three-dimensional structure of the lungs, physiological functions and pathological mechanisms. *Approach.* This work presents both synchrotron and laboratory XPCT results of postmortem tissue from autopsies and biopsies embedded with various preparation protocols such as precision-cut lung slices, cryogenically fixed lung tissue, as well as paraffin and alcohol fixed tissue. The selection of pathological abnormalities includes channel of Lambert, bronchus-associated lymphoid tissue and alveolar capillary dysplasia with misalignment of pulmonary veins. Subsequently, quantification and visualization approaches are presented. *Main results.* The overall high image quality even of in-house XPCT scans for the case of FFPE biopsies can be exploited for a wide range of pulmonary pathologies and translated to dedicated and optimized instrumentation which could be operated in clinical setting. By using synchrotron radiation, contrast can be further increased to resolve sub-μm sized features down to the sub-cellular level. The results demonstrate that a wide range of preparation protocols including sample mounting in liquids can be used. *Significance.* With XPCT, poorly understood 3D structures can be identified in larger volume overview and subsequently studied in more detail at higher resolution. With the full 3D structure, the respective physiological functions of airways or vascular networks, and the different pathophysiologic mechanisms can be elucidated or at least underpinned with structural data. Moreover, synchrotron data can be used to validate laboratory protocols and provide ground truth for standardizing the method.

1. Introduction

The lung is a perfect example of how the function of an organ is enabled by its three-dimensional (3D) structure, here formed by intricate and intertwined networks of ventilation and vasculature. In radiology, the lung is

known as a high contrast organ for radiography and computer tomography (CT), and quite a number of lung diseases can readily be diagnosed from radiographs or CT scans, such as infections, emphysema or fibrosis. The 3D structure of the lung cyto-architecture is again key to physiology and pathophysiology, i.e. the cellular and the histological level. Histological diagnostics at much higher resolution than radiology is advantageous for a range of non-neoplastic lung diseases, such as interstitial lung diseases, pulmonary vascular diseases, virus induced pneumonia, fibrosis or other displastic pathologies. To this end, histomorphological assessment of formalin-fixed, paraffin embedded (FFPE) thin tissue sections, stained with haematoxylin and eosin still represents the gold standard. However, the functional cyto-architecture of the lung parenchyma is often insufficiently captured in 2D, and 3D visualisation and quantification of the morphological changes associated with different pathologies and diseases could significantly improve and complete the diagnosis.

To this end, it is by now well appreciated that propagation-based x-ray phase-contrast tomography (XPCT) offers a unique potential to extend histology and pathohistology. It promises a scalable, isotropic resolution without destructive slicing of the specimen and quantitative density-based contrast (Khimchenko *et al* 2016, 2018, Saccomano *et al* 2018, Töpperwien *et al* 2018, Dejea *et al* 2019, Ding *et al* 2019, Eckermann *et al* 2020, Westöö *et al* 2021, Barbone *et al* 2022, Palermo *et al* 2022).

Recent work has significantly improved the classic phase retrieval approaches (Paganin and Nugent 1998, Cloetens *et al* 1999, Alloo *et al* 2022), for example by nonlinear generalizations and Tikhonov regularization (Lohse *et al* 2020, Huhn *et al* 2022). Furthermore, scans with highly coherent synchrotron radiation both in the parallel beam settings with high resolution scintillator-based detector systems, and in magnifying cone-beam settings now routinely reach the micron and sub-micron resolution range, respectively, down to voxel sizes around 100 nm, which can even be implemented in the same instrument (Frohn *et al* 2020), and at least partly in high throughput (by continuous scans and detector readout).

Lung imaging by XPCT has early on been implemented on macro- and microscopic scales (Parsons *et al* 2008, Leong *et al* 2014, Stahr *et al* 2016, Bayat *et al* 2020, Morgan *et al* 2020, Borisova *et al* 2021, Shaker *et al* 2021, Bayat *et al* 2022a, 2022b, O'Connell *et al* 2022), including even live animal models of respiratory diseases. At the histological level, we have recently used multi-scale XPCT to image the parenchymal architecture of unstained FFPE lung tissue of patients who succumbed to COVID-19 (Eckermann *et al* 2020). The 3D reconstructions provided visualisations of diffuse alveolar damage (DAD) with its prominent hyaline membrane formation, mapping the spatial distribution and density of lymphocytes infiltrating the tissue, vascular damage and intussusceptive angiogenesis, as well as distance histograms from tissue interior to the closest air compartment.

In this work, we extend virtual 3D histology and pathohistology of lung by XPCT to a wider range of pathologies. We investigate how the mounting and embedding as well as different setups and implementations affect the image quality. We provide benchmark reconstructions and illustrative examples, including both synchrotron radiation (SR) and compact μ-focus sources. The latter is particularly relevant for potential dissemination, as laboratory instrumentation is more accessible for pathology units. A central goal of this work is to support the assertion that integration of 3D morphological information with well established histology techniques helps to unravel the pathophysiology of lung diseases, as previously shown for COVID-19. Furthermore, future extension could possibly also cover advanced clinical diagnosis. As a fist step, we here provide XPCT results for postmortem tissue from autopsies as well as for biopsies in the context of different pathologies. Finally, we include first XPCT results on cultivated lung tissue, namely precision-cut lung slices (PCLS), in this study, as well as CT results of cryogenically fixed lung tissue.

The manuscript is organized as follows: after this introduction, methods of sample preparation and image acquisition both with SR and μ-CT are detailed, as well as the analysis workflow. In the following the results are presented for paraffin- and liquid embedded (channel of Lambert, bronchus-associated lymphoid tissue, alveolar capillary dysplasia with misalignment of pulmonary veins) samples as well as for precision cut lungs slices and cryogenically fixed tissue, respectively. Subsequently, quantification and visualization approaches are presented while the manuscript concludes with a discussion of the results.

2. Methods

2.1. Sample preparation

2.1.1. Fixation in liquid media

To prevent freshly dissected tissue samples from deterioration, uncontrolled drying and deformation, chemical fixation is required after extraction. Formaldehyde (formalin) is commonly used as a highly protein-cross-linking fixative, but dehydration in alcohol can also be used as a non-carcinogenic and less hazardous substitute. Because it does not cross-link molecular groups, it also facilitates immunohistochemical studies (van Essen *et al* 2010). For liquid embedding in this work, freshly prepared samples, which were several cubic centimeters in size, were placed in 98% alcohol solution (2% Phosphate-buffered saline (PBS)), and wrapped with absorbent cotton

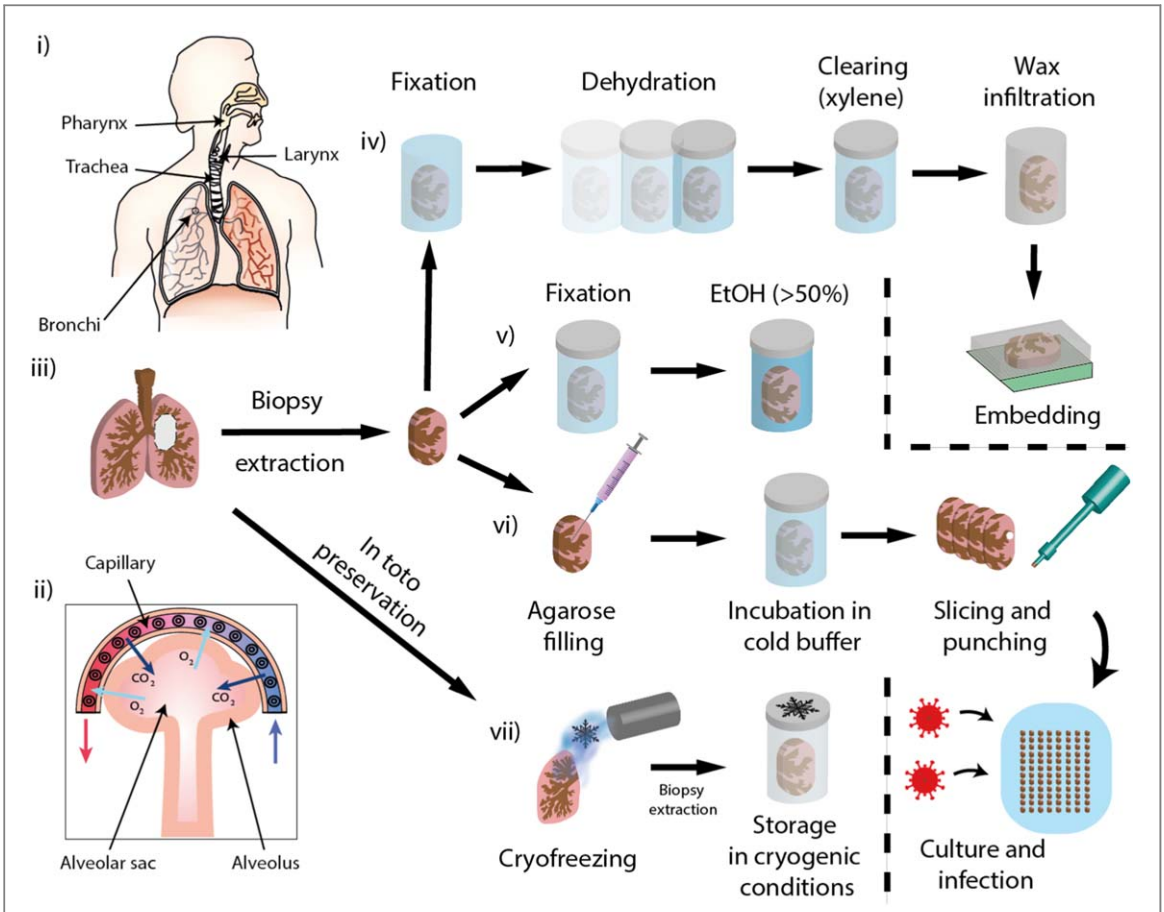

Figure 1. Lung biopsy extraction, preparation and mounting for XPCT. (i) Schematic of the human respiratory system. (ii) Illustration of the alveolar sac as the terminal point of the airway. CO_2 from deoxygenated blood diffuses into the alveolar sac, while O_2, collected by ventilation, diffuses back into the capillary, thereby oxygenating the blood. (iii) Tissue samples were extracted from the human lung by a biopsy needle/biopsy punch, during clinical intervention for diagnostic purposes, or post mortem during autopsy. (iv) Workflow for paraffin-embedding of samples (fixation, dehydration, clearing, wax infiltration). (v) Fixation in ethanol (98%, 2% buffer). (vi) Cryogenic fixation of samples with liquid nitrogen vapors. (vii) Preparation of PCLS by filling the sample with agarose, incubation in cold buffer, slicing and punching and subsequent intentional infection while in cultivation.

to avoid sample movement during image acquisition (figure 1(v)). An example can be found in the supplemental document.

2.1.2. Paraffin-embedding

Formalin-fixed paraffin-embedded (FFPE) tissue is the most common embedding and preservation procedure in clinical pathology, and has already been successfully used for 3D virtual histology of lung with synchrotron and laboratory radiation (Eckermann *et al* 2020). For this experiment, tissue fixation, embedding and mounting were performed according to existing protocols (Töpperwien 2018). Further details on the preparation protocol can be found in the supplemental document.

2.1.3. Precision cut lung slices

In this work, we include first results on PCLS by XPCT study, in order to explore if XPCT could potentially support PCLS research by 3D imaging. To this end, different sample preparation protocols and imaging conditions have been tested. More details on the preparation protocol and the selection of samples can be found in the supplemental document.

2.1.4. Cryogenic fixation

Immediately after tissue collection, the lung can be frozen *in toto* to preserve delicate structures (figure 1(vii)). By applying water-controlled air pressure, the lung is inflated and the pressure lowered to achieve an uniform recruitment of the lung specimen. The lung is then placed in a styrofoam box and frozen in liquid nitrogen vapors. At this point, the lung can be safely stored at −80 °C until further use (Verleden *et al* 2022). While this technique was previously applied in combination with commercially-available in-house micro-CT scanners

(Campbell *et al* 2012, Vasilescu *et al* 2017, Maes *et al* 2022), to our best knowledge this study is the first to scan macroscopic cryo-fixed biological tissue with synchrotron radiation.

2.2. Experimental setup

2.2.1. Laboratory-based μ-focus sources

Synchrotron radiation (SR) sources offer highly brilliant beams of high lateral and longitudinal coherence, ideally suited for XPCT. Monochromaticity on the order of $\Delta\lambda/\lambda \simeq 10^{-4}$ is achieved by single crystal monochromators; a wide range of beamline optics typically support collimated beams (parallel beam geometry) or a secondary focus with cone beam illumination of the sample. However, since the availability of SR is restricted to just a few sites and selective allocation of beamtime, translation of XPCT to setups operated at laboratory sources, namely μ-focus x-ray tubes (with spot sizes down to the sub-micron range) is of paramount importance for daily preclinical research and future clinical applications. Since spatial coherence is a prerequisite for phase sensitivity, the lateral coherence length $\xi = \lambda x_{01}/\sigma_s$ must at least exceed the effective pixel size. This is possible at high resolution (small pixel size), if the source-sample distance (x_{01}) and the effective wavelength λ representing the spectrum are sufficiently large, and the source size σ_s is sufficiently small. This was first achieved by the advent of liquid metal jet anodes (Hemberg *et al* 2003), which enabled XPCT scans and reconstructions (Bartels *et al* 2013), and later by compact laser-driven synchrotron sources (inverse Compton sources) (Eggl *et al* 2015). More recently, more compact μCT instruments even with solid targets and spot sizes around a few microns or even in the sub-micron range (denoted as nanofocus sources by vendors) have reached sufficient partial coherence for XPCT of soft biological tissue (Eckermann *et al* 2019, Massimi *et al* 2019, 2021). In this work, differently prepared human lung tissue samples were scanned at a commercially μCT system (LS1-setup) as well as a custom built in-house CT instrument (LS2-setup). Details on instrumentation and acquisition parameters can be found in the Supplementary Document.

2.2.2. XPCT with synchrotron radiation

For applications requiring highly brilliant and monochromatic x-ray beams, SR is the best choice. Quantitative phase retrieval is possible based on the much higher coherence and multiple length scales can be covered down to sub-100 nm resolution. In this work we took advantage of a multiscale XPCT approach, using both the parallel (SR1) and cone beam (SR2) configurations of the GINIX endstation installed at the P10 beamline of the PETRA III storage ring (DESY, Hamburg) (Frohn *et al* 2020). The GINIX endstation is dedicated to propagation-based holographic tomography of biological samples, and operates in the medium to hard x-ray regime (5–14 keV). For high resolution (cone beam) recordings, the beam was focused by a pair of Kirkpatrick-Baez (KB) mirrors and further reduced by a germanium x-ray waveguide, which also increases the spatial coherence of the propagated x-ray wave by mode filtering (Salditt *et al* 2015). Two configurations can be used at the same beamtime and were used in this work to investigate lung tissue at multiple scales. Details on the setup and acquisition parameters can be found in the supplementary document.

For exploiting the multi-scale capabilities of XPCT, biopsy punches were taken from the paraffin embedded samples with diameters varying from 4 mm (overview of the sample) to 1 mm (high resolution scans). To achieve a large FOV, samples with diameters larger than 1 mm are examined with a parallel beam geometry (1.6 $\times$ 1.4 mm) or a cone beam geometry at the LS1-setup. Here, the magnification and therefore the FOV depends on the setup geometry. By increasing x_{12} or decreasing x_{01} (figure 2) a magnification resulting in a smaller effective pixel size can be achieved. Since the difference in attenuation between paraffin and soft tissue is about three magnitudes lower compared to the induced phase shift, paraffin tends to be a very suitable embedding material for XPCT when it comes to biological soft tissue. In the course of this work, different pathologies were investigated to illustrate the capabilities of XPCT for 3D imaging of lung tissue, and to suggest suitable experimental configurations, depending on preparation type and application.

2.3. Data reconstruction and post processing

For experiments at the synchrotron (SR) as well as the custom-built laboratory setup (LS2), data acquisition was immediately followed by phase- and tomographic reconstruction.

Phase reconstruction was carried out assuming a homogeneous, weakly absorbing object using the linearized single step CTF-approach (Cloetens *et al* 1999, Krenkel *et al* 2015) or nonlinear Tikhonov (Huhn *et al* 2022b) at the synchrotron assuming a low Fresnel number ($F = a^2/(x_{12}\lambda)$, where a is the characteristic size of the object and x_{12} the propagation distance) resulting in a holographic regime. In the laboratory, to preserve image sharpness the transport-of-intensity equation based Bronnikov-aided correction (BAC) scheme is used (Witte *et al* 2009, Töpperwien *et al* 2016).

For the tomographic reconstruction, the projections were flat- and dark field corrected with the *iradon* function implemented in MATLAB using a Ram-Lak filter for backprojection. To increase the signal-to-noise

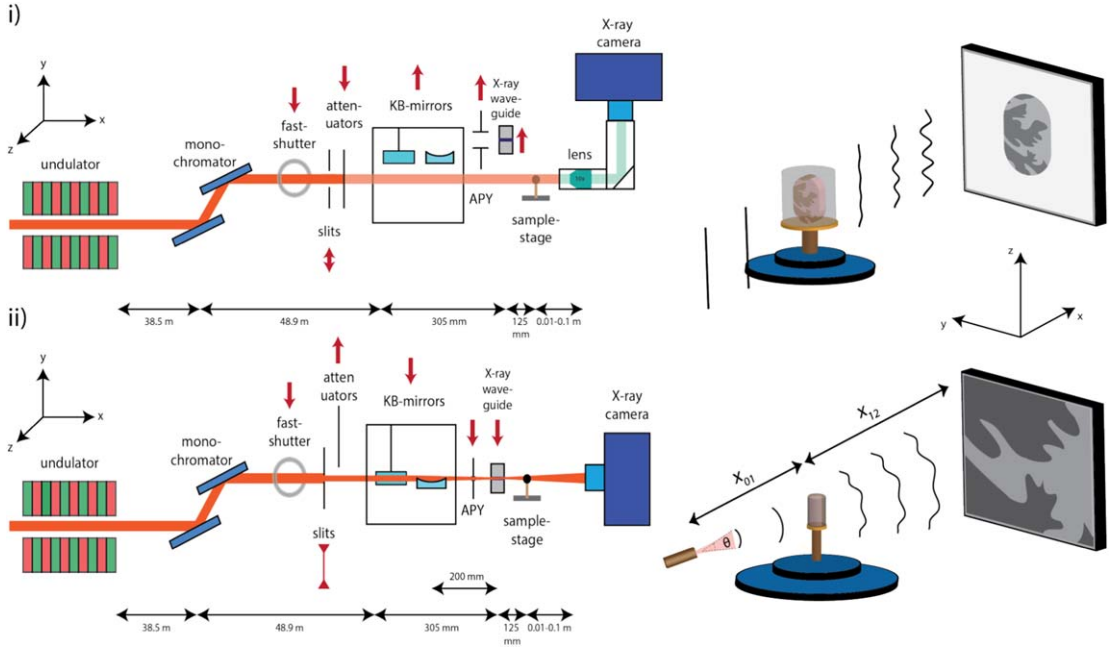

Figure 2. Optical layout of the GINIX instrument. The configuration can be switched between (a) a parallel beam geometry, and (b) cone beam beam geometry. For (a), polished single crystal attenuators are inserted in the unfocused synchrotron beam to avoid detector overexposure. KB-mirrors and the waveguide are moved out of the beam path. A microscope detector system (Optique Peter) equipped with an sCMOS camera (PCO.edge) was used. The detector system was used with a 50 μm Lu:Ag scintillator, and a 10x objective) resulting in $px = 0.65$ μm. For the configuration shown in (b), the beam is focused by KB mirrors down to about 300 nm $\times$ 300 nm. After passing an aperture (APY), the beam is coupled into an x-ray waveguide, aligned in the focal plane of the KB. After exiting the waveguide, the broadened beam with opening angle θ illuminates the sample positioned at distance x_{01} behind the waveguide exit, and projection images are recorded in the detection plane at distance x_{02}, with a fibre-coupled scintillation detector (Zyla HF 5.5, 15 μm Gadox scintillator, fiber optic plate coupled to sCMOS, $px = 0.65$ μm).

ratio at in-house setups, several projections (# accumulations in supplementary table 1) were taken at the same rotation position and averaged directly after acquisition was completed. Fresnel numbers were verified and if needed refined by inspecting the radially averaged PSF of a hologram to the expected CTF and according re-scaling. Additionally, a wavelet-based filtering approach was applied to further mitigate ring artifacts occurring during the reconstruction (Münch *et al* 2009). All used algorithms are implemented in our code package HoloTomoToolbox (Lohse *et al* 2020). At the commercial nano-CT device (LS1), reference images (additional images at different angles before and after the scan) were taken to account for source spot movement by autocorrelation with tomographic projections and the rotation axis was corrected. Ring filter correction and phase retrieval algorithm were applied before tomographic reconstruction. The phase retrieval parameter were set manually after eye inspection.

Fiji (Schindelin *et al* 2012) and MATLAB (R2020a) were used for further analysis and NVIDIA IndeX (NVIDIA Corporation, Santa Clara, CA, USA) (Schneider *et al* 2021) for rendering of the volumes. Video sequences and further renderings were created using the Avizo software (Thermo Fischer Scientific, Waltham, CA, USA).

3. Experimental results

3.1. Channel for collateral ventilation

Figure 3 presents images of a channel of Lambert, an important bypass airway relevant for collateral ventilation. Images were obtained on an unused donor lung with mild emphysema which we examined by a parallel beam geometry as well as with waveguide optics using synchrotron radiation (GINIX, PETRA III, Hamburg). For the former, nine volumes were recorded in a plane with a sufficient overlap to stitch the volumes together (AVIZO, Thermo Fisher Scientific, Berlin) during post-processing. This resulted in an extended FOV of about 3.8 mm and thus allowed to investigate the 3.5 mm punch in its full diameter to observe an interbronchiolar channel (channel of Lambert) which usually has a diameter of around 30 μm and can be found between respiratory and terminal bronchioles of adjacent segments (Martin 1966). This morphological feature enables so-called collateral ventilation which serves to compensate for imbalances between ventilation and perfusion, as they occur in many diseases. It has been speculated that collateral ventilation can increase in response to emphysema,

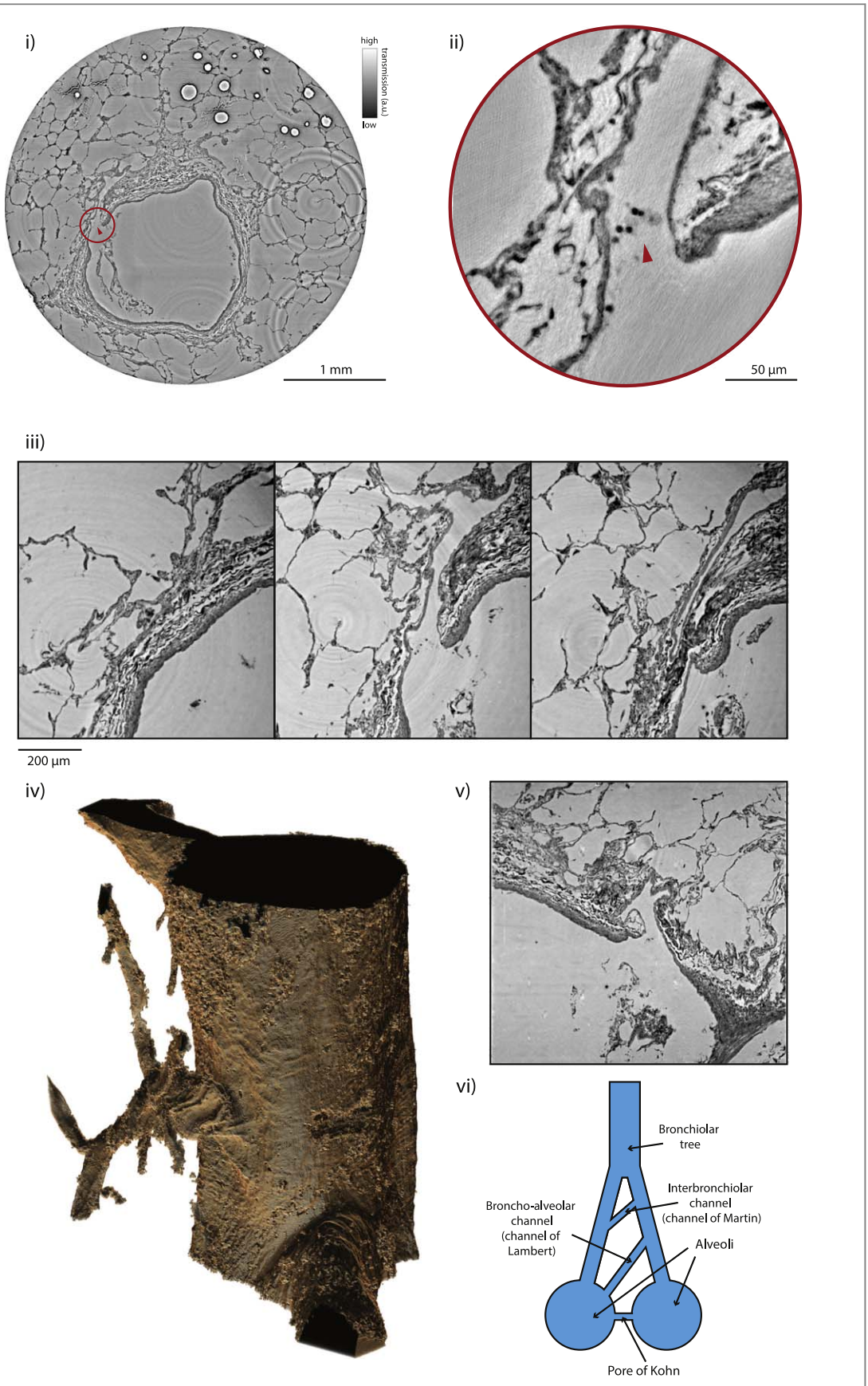

Figure 3. Channel of Lambert. (i) Stitched volume of nine datasets with a FOV of ≈ 4 mm, 2 × 2 binning and a resulting effective voxel size of 1.3 μm (SR1-setup). Slice through *xy*-plane, depicting two bronchioles and the opening of an interbronchial channel (channel of Lambert, red square) (scale bar: 1mm). (ii) High resolution scan of ROI with x-ray waveguide (SR2-setup), resulting in a FOV of 0.32 mm × 0.27 mm and an effective pixel size of 125 nm. Tikhonov regularisation was used for phase reconstruction (scale bar: 50 μm). (iii) Series of transaxial planes depicting the channel of Lambert (scale bar: 200 μm). (iv) 3D rendering of the segmented volume with a focus on the interbronchial channel. (v) Orthogonal slice depicting the ROI. (vi) Illustration of a transbronchial tree with respiratory and terminal bronchioles.

either opening up new flow channels for flow or causing enlargement of existing channels, and thereby reducing their resistance (Cetti *et al* 2006). Emphysema is defined as an increase beyond the normal in the size of the air spaces distal to the terminal bronchiole and is associated with the destruction of septae (Cetti *et al* 2006). However, up to now, channels of Lambert were not yet depicted and quantified in its full three-dimensionality. Therefore, they could not be properly compared to other ways of collateral ventilation (figure 3) and their role in gas exchange both in normal and disease states still remains largely unknown (Terry and Traystman 2016). With the advent of XPCT which can now provide the required 3D data this situation has changed.

3.2. Bronchus-associated lymphoid tissue

In the next example, we show results for bronchus-associated lymphoid tissue (BALT) after a SARS-CoV-2 infection obtained in-house with the LS1 setup. Figure 4 presents a representative slice through the reconstruction volume, and a rendering of structures of interest. BALT describes a localized, intrapulmonary accumulation of lymphatic cells in the lungs and bronchus that participate in airway immune responses and are located on the airway mucosa. It is frequently found between airways and arteries (Meyerholz *et al* 2018) and often within the walls of large airways (Sminia *et al* 1990). While BALT is similar in most mammal species, it differs in maintenance and inducibility, and appears in mice or humans only after infection or inflammation (Tschernig and Pabst 2000). Favouring factors for the presence of BALT in human adults include infection, pathogen exposure, chronic pulmonary inflammation or autoimmune disease (Ak 2021). It can further harbor an overall rare type of extranodal marginal zone lymphoma, mostly present in primary non-Hodgkin lymphoma (NHL). In view of their role in immune response and pathology, investigations of BALT formation in human lung biopsies are highly relevant and could be enhanced by 3D information from XPCT. As we show here, BALT and lymphoid proliferation can be detected using the in-house LS1-setup (figures 4(i), (ii)). By scanning the same pathology using the SR1-setup (figure 4(iii)), we observe that the lymphoid nodes seem to be filled with lymphocytes which potentially entered the lumen by high endothelial venules facilitated by pulmonary inflammation or immunization (Sato *et al* 2000) caused by a SARS-CoV-2 infection. These structures are usually studied by transmission electron microscopy, at high resolution but only on two-dimensional sections. In-house XPCT, however, can produce a high contrast three-dimensional dataset in just a few hours, providing the possibility of a fast segmentation of features of interest (figure 4(iv)), allowing to study the distribution of the lymphoid tissue as well as their shape, orientation and preferred area of accumulation.

3.3. Alveolar capillary dysplasia with misalignment of pulmonary veins

Figure 5 presents another example of human lung tissue, where we studied alveolar capillary dysplasia with misalignment of pulmonary veins (ACD/MPV), first again using paraffin embedded lung tissue, scanned with a parallel beam at the SR1-setup as well as in liquid media at an in-house setup (LS1-setup). The term ACD/MPV describes a rare, fatal lung developmental disorder, affecting the alveoli and their surrounding capillaries resulting in an impaired gas exchange. According to Bishop *et al* (2011), it is commonly distinguished by immature lobular development, reduced capillary density, abnormal air-blood barriers and anomalous veins in bronchovascular bundles. Historically, it was suggested that the fetal lung vascularization leads to a significant reduction of pulmonary capillaries forcing the blood entering an individual lung to drain via misaligned veins (Bishop *et al* 2011). However, in a recent work, Norvik *et al* were able to show that these suspected veins indeed represent dilated bronchopulmonary shunt vessels (in their designated position). Therefore, the term MPV seems to be a misnomer (Norvik *et al* 2020). Presumably, the clinical course is strongly influenced by the severity of disruption in capillary density and their lack of contact with the alveolar epithelium (Melly *et al* 2008). In severe cases, the sum of the pathologies result in respiratory failure with a nearly 100% mortality rate (Deutsch *et al* 2007). While chest x-rays may already give some indications for the pathology, they can easily be misinterpreted as normal. Biopsies, on the other hand, can be used to diagnose ACD/MPV. Further, in order to gain a more complete understanding of the disease, a three-dimensional imaging technique such as XPCT may add a significant benefit, by shedding light on the underlying histopathological manifestation of the condition.

The samples used in the study were extracted from ethanol-fixed fresh human lung tissue of one ACD case. Bronchi and vasculature could be easily detected and segmented so that their course becomes observable. Notably, the artery and the shunt vessel show parallel, wavelike structures at the bottom of the rendered volume (figure 5(ii)). The histological slice align almost perfectly with the virtual slice, allowing to study the immunochemical properties at specific regions of interest (figure 5(iii)).

3.4. Precision cut lung slices

Respiratory diseases are among the leading causes of death, closely following stroke and cancer (Ritchie *et al* 2018). However, in contrast to cardiovascular diseases and tumors, respiratory pathologies suffer from a deficit in translatable animal models. This compromises the development of efficient therapies, and creates to use

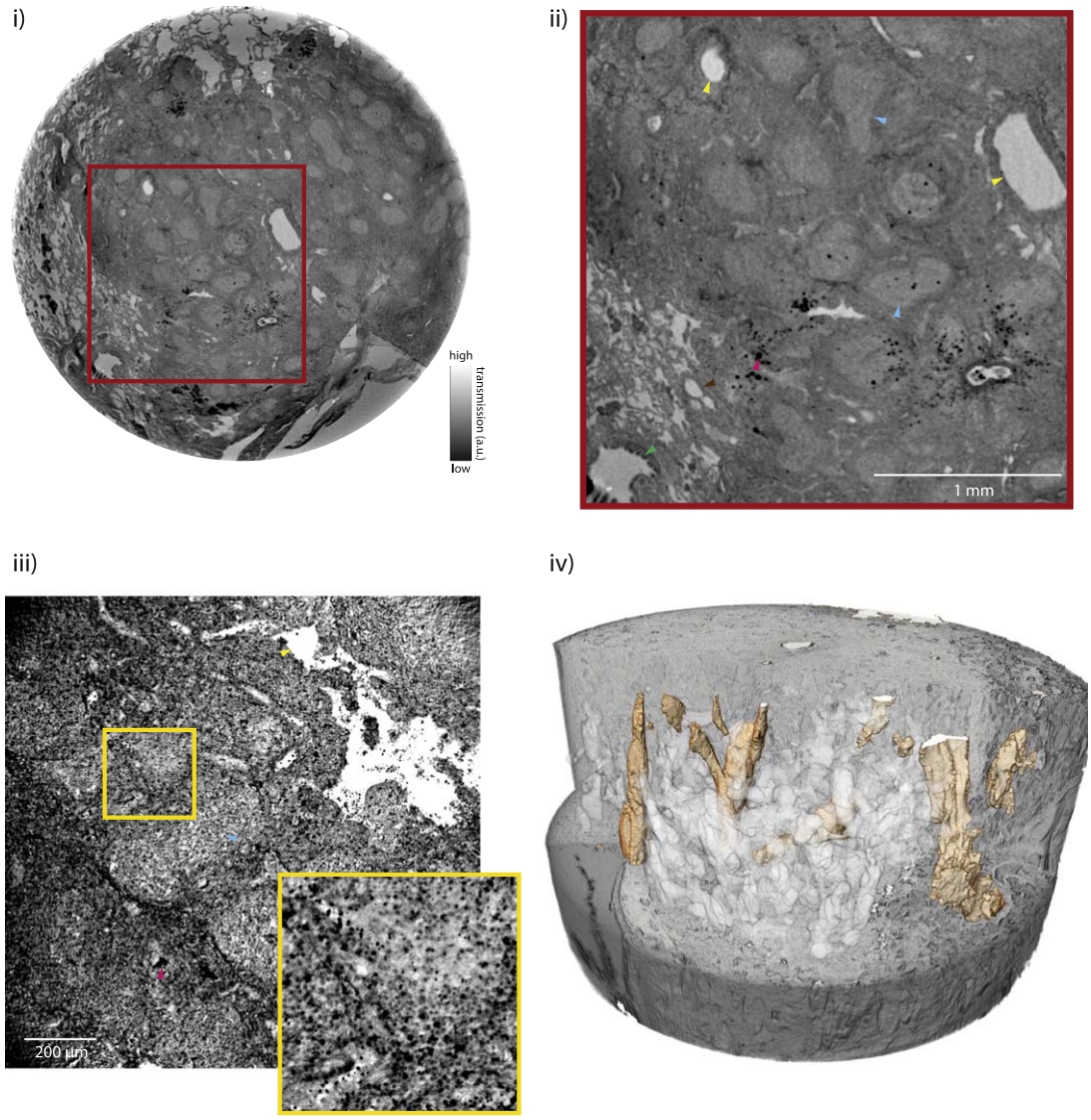

Figure 4. Bronchus-associated lymphoid tissue (BALT). (i) In-house recorded (LS1-setup) paraffin-embedded sample (3.5 mm diameter) of a patient with BALT, showing the entire FOV. Images were recorded with the microfocus transmission source of the LS1-setup equipped with a tungsten target (instead of the nanofocus source with LaB6 cathode available at the same instrument), offering a significantly larger spot size (7–50 μm) and hence power. (ii) Zoom to a region of interest. The entire biopsy punch has a diameter of ≈5.6 mm. Arrows mark specific features of interest. Blue: Lymphoid tissue, Green: Bronchus, Yellow: Veins/arteries, Brown: Alveolar sacs (Supplementary table 1: LS1 BALT, scale bar: 1 mm). (iii) Paraffin-embedded 3.5 mm punch recorded with the SR1 setup. The reconstructed volume reveals a high accumulation of cell nuclei and lymphocytes within and surrounding the bronchiolar lymphoid tissue (scale bar: 200 μm). (iv) 3D rendering with segmented out vasculature and lymphoid tissue.

human cell lines to model the pathology. Despite many recently established techniques such as transwell systems (cell co-culture environment mimicking *in vivo* conditions) and 'organ-on-a-chip' systems, many drawbacks and problems with translatability still persist. More recently, Precision Cut lung slices (PCLS) were proposed as a potential solution, with slices being cultured from explanted or diseased human lungs, containing all cell types from the tissue of interest including the extracellular matrix (Liu *et al* 2019). Until now, the PCLS system has already provided insights into various pulmonary diseases such as asthma (Torgerson *et al* 2011, Kennedy *et al* 2018), COPD (Bauer *et al* 2010, Donovan *et al* 2016), idiopathic pulmonary fibrosis (Mercer *et al* 2016, Alsafadi *et al* 2017) as well as infections (Temann *et al* 2017). Furthermore, it is favourably utilized for testing of efficacy and safety of new therapeutic targets (Martin *et al* 1996, Cooper and Panettieri 2008). In the process of enabling a structure-preserving extraction of lung tissue, a standardized protocol was recently established (Gerckens *et al* 2019), promising a near-native environment and allowing reliable high-throughput analysis of drugs and viruses.

Figure 6 presents first (preliminary) x-ray imaging examples of PCLS, related to a recent project, addressing SARS-Cov-2 infection in the PCLS model (Ricke-Hoch *et al* 2021). Lung samples prepared by different protocols

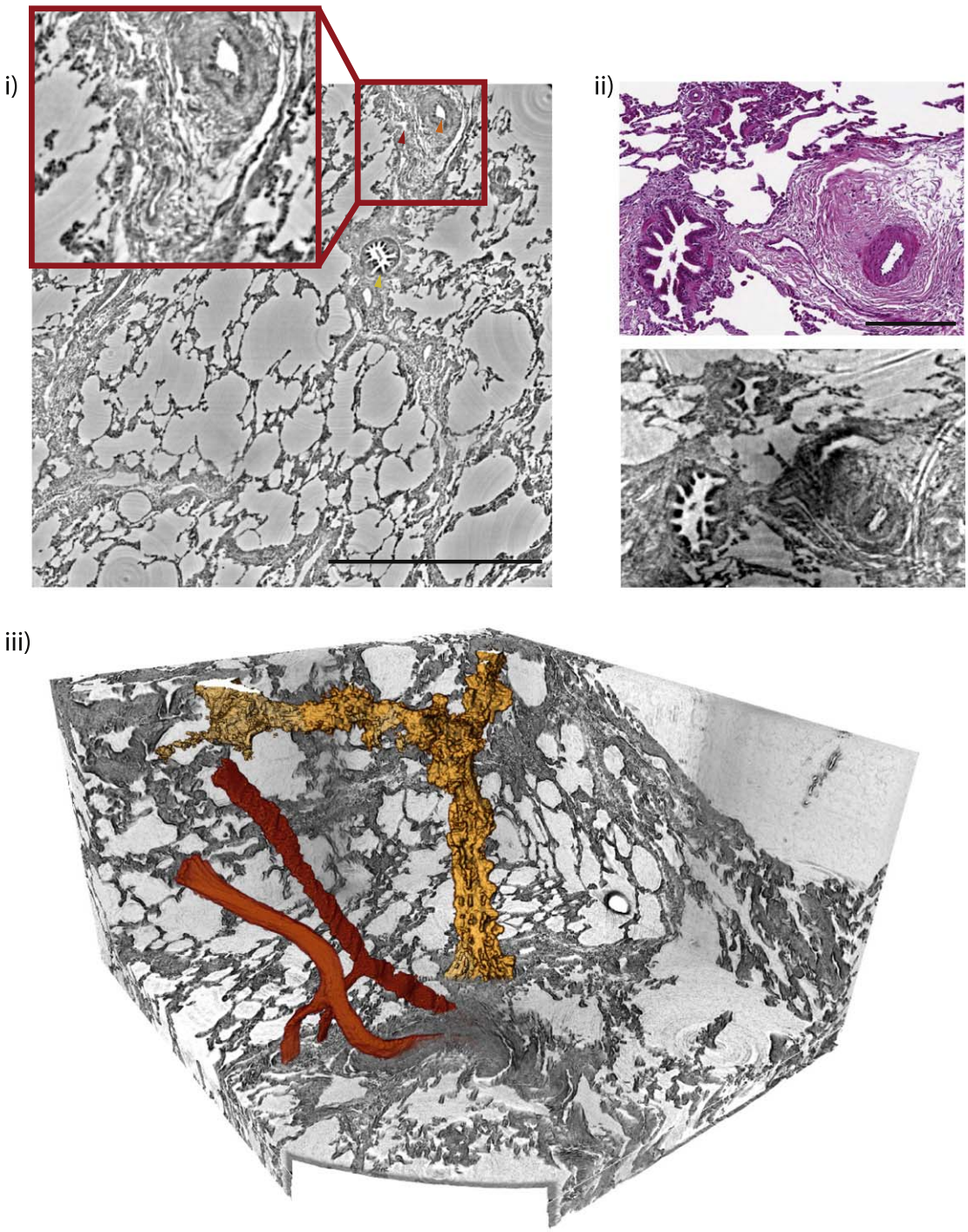

Figure 5. Alveolar capillary dysplasia (ACD). (i) Selected slice (FOV: ≈ 2.5 × 2.5 mm, 1.3 μm voxel size) with a bronchovascular bundle from patients with ACD scanned at the SR1-setup. Coloured arrows indicate features of interest (red: bronchi, orange: artery, red: shunt vessel, scale bar: 1 mm). (ii) 3D illustration of the segmented bronchus, artery and shunt vessel (same color code as in (i)). (iii) Correlation of XPCT reconstruction with H&E stained histological slices can be performed after the non-destructive XPCT scan within a well chosen region of interest (scale bar: 200 μm). Acquisition settings are tabulated in supplementary table 1: LS1 ACD-MPV and supplementary table 2: SR1.

and mounted in different media, as described in section 2.1) were scanned at different modalities and in different configurations. The results show that high contrast is obtained even at in-house setups for critically point dried samples, see figures 6(i)–(iii). However, as a downside of this method, as expected the tissue morphology is strongly affected by dehydration, resulting not only in shrinkage but also rupturing of the tissue. Also, due to the very high phase contrast between dried tissue and air edges, the contrast even with laboratory sources, but certainly for synchrotron scans, may even be too strong to perform successful phase retrieval, at least for most of the conventional phase retrieval approaches. For the in-house scans, one can chose a configuration with large propagation distance and magnification with a detector of larger pixel sizes as shown in (ii) for a scan of larger

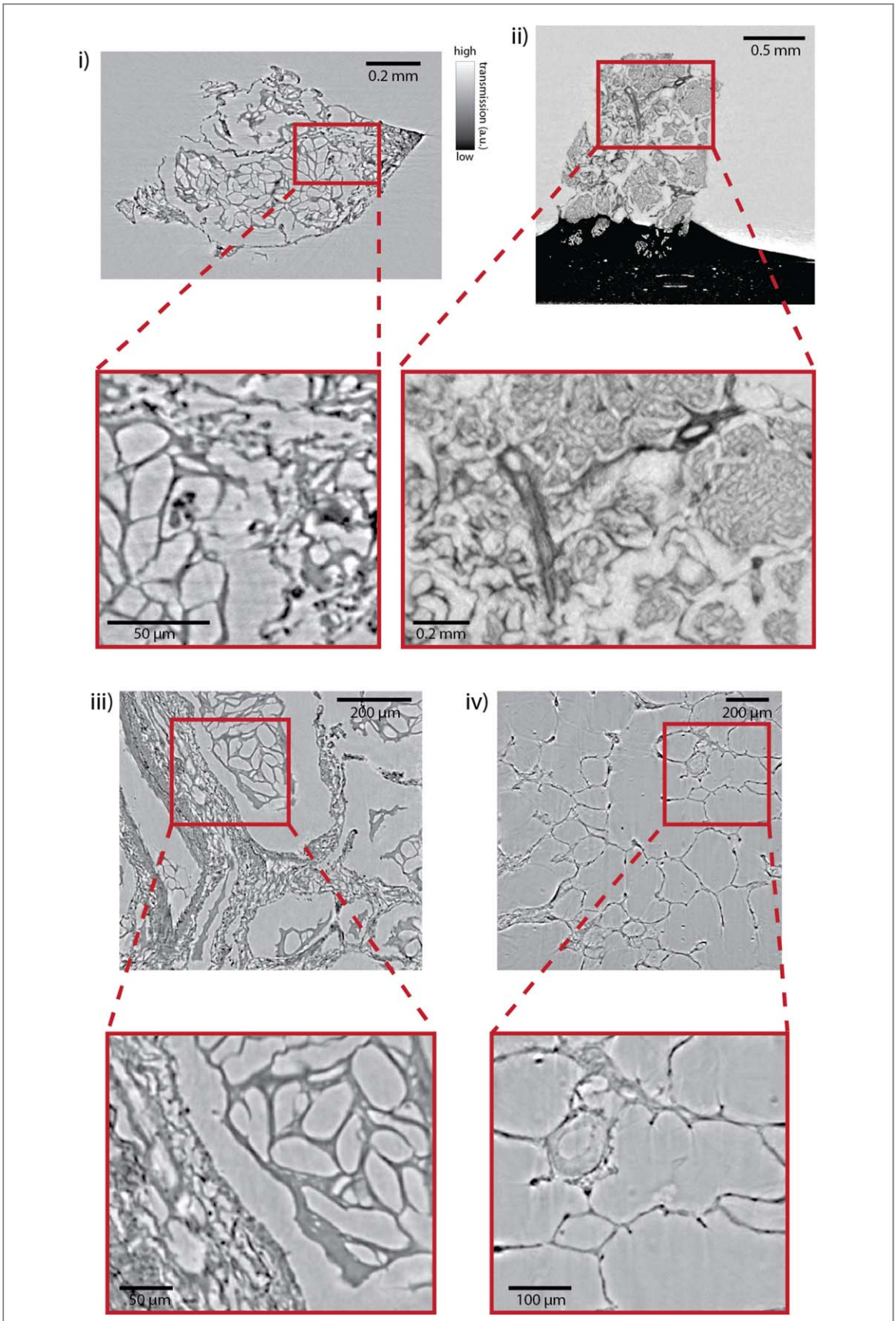

Figure 6. Precision cut lung slices (PCLS), imaged under different preparation protocols and imaging parameters/setups: (i) critical point dried PCLS sample, measured at the LS2-setup (Supplementary table 1: LS2 PCLS Argos, scale bar (zoom): 0.2 mm (50 μm)). (ii) Critical point dried PCLS measured in-house at the LS2-setup (supplementary table 1: LS2 PCLS Pirra, scale bar (zoom): 0.5 mm (0.2 mm) (iii) Detailed Critical Point dried sample measured with the LS1-setup (supplementary table 1: LS1 PCLS, scale bar (zoom): 200 μm (50 μm)). (iv) Unexposed liquid-embedded control sample scanned with a parallel geometry at the SR1-setup (supplementary table 2, scale bar (zoom): 0.2 mm (100 μm)).

FOV, here obtained at the LS2 setup. Alternatively, at the same instrument one can chose a detector with very small pixel size, see (i), where the Argos detector with $px = 0.54$ μm is positioned very close to the sample, which allows us to have much higher resolution, at the cost of much longer acquisition time. Finally, at the commercially available in-house setup LS1 consisting of a solid target source (iii) and a CCD detector with medium sized pixel sizes $px = 9$ μm, appropriately chosen geometric parameters x_{01} and x_{12} (see supplementary table 1). This allowed us to achieve a high contrast in the reconstructed slices while having a resolution comparable to the LS2 PCLS setup with the high resolution camera Argos. Finally, liquid embedded *ex vivo* samples scanned with synchrotron radiation (SR1) clearly reveal a well resolved and well-preserved alveolar network. It can be concluded that the specimen remained largely undamaged during the challenging sample preparation process of thinly sectioning the tissue with a microtome.

3.5. Imaging cryogenically fixed samples

Following mountings in paraffin (FFPE-tissue blocks), liquid embedding, and critical point drying, we now turn to cryogenic fixation, which—if cryo-cooling is sufficiently fast—can be expected to preserve the tissue structure well and also preserves the natural tissue-air contrast . After cryogenic fixation of the lung in an inflated state, the sample was placed into the path of the parallel beam setup at the P10 beamline (LS1). To this end, a custom-made box, consisting of a self-fabricated plastic body, a circular shaped polyimide (Kapton) foil and a perforated lid, was used. Directly after taking the samples out of the cooled chamber, they were placed on a metal pin (Huber Diffraktion-stechnik) and inserted into the box. Dry ice was put into the perforated lid, which was subsequently placed onto the Kapton foil to ensure that the sample was not exposed to room temperature for too long. The dry ice evaporated and thus cooled the sample directly underneath, see figure 7(i).

The results can be inspected in figure 7, where two slices from a lung with pediatric pulmonary hypertension are displayed with perpendicular orientations. The xy-slice appears to have parallel, horizontal stripes which are an indication for sample movement during the scan (iii). This can be attributed to shrinkage of the tissue due to a non-ideal setup and a temperature in the box of -15 °C which might be not sufficient to maintain the sample frozen for the duration of the data acquisition. However, as expected, the strong contrast caused by a large difference in electron density between tissue and air allows to achieve a very high contrast, which is a challenge for phase retrieval and is likely to compromise the image quality regarding the detailed structure of the alveolar septae. Contrarily, the high contrast enables a straightforward, threshold based tissue segmentation of the septa, see (iv). A comparison with the same cryogenically fixed sample imaged with a commercially available in-house scanner shows the strong increase in resolution and contrast achieved with synchrotron radiation, compare (ii) and (iii). Importantly, in contrast to paraffin- or alcohol-embedded samples, the tissue appears to be barely damaged and may best represent the real alveolar and tissue structure in an intact organism.

3.6. Quantification of virtual histology datasets

After presenting examples of XPCT reconstructions of illustrative lung tissue samples, highlighting different pathologies imaged with advanced in-house and synchrotron setups, we now consider automated quantification by 3D metrics of tissue structure. By automated computation of morphometric parameters, tissue features can be assessed in an objective manner without human visual judgement. Given proper validation with current pathological assessment and interpretation, large volumes can be interrogated and patterns representing pathological manifestations could be identified. To this end, we want to put forward two approaches, which we consider particularly well suited to quantify lung tissue in a generic manner, namely firstly the so-called chord length distribution (CLD), and secondly the structure tensor approach. CLD which has already proven to be a valuable concept to characterize pore size distributions of concretes (Chung *et al* 2020) and (polychrystaline) microstructures (Turner *et al* 2016, Latypov *et al* 2018), but also to assess the morphology of the lung based on two-dimensional sections (Knudsen *et al* 2010, Crowley *et al* 2019).

3.6.1. Chord length distribution

Figure 8 presents the CLD analysis. As a proof of concept, the chord length distribution is calculated here for a young lung donor without any known preconditions and an old donor, also with no known preconditions apart from age-related decay (laboratory scan: figure 8(i); synchrotron scan: figure 8(iii)). In both cases, chemically fixed paraffin embedded samples were prepared and scanned. First, the volume recorded with LS1-CLD setup is binarized using a manually determined optimal threshold and morphological operations which are applied to filter out artifacts and to correctly distinguish tissue from paraffin. In this way, the volume was separated in two phases (tissue: phase 1; paraffin: phase 0). Secondly, a slightly modified, already available, MATLAB-function (MacIver and Pawlik 2017, MacIver 2022) was used to calculate a distribution of chord lengths by creating directional anisotropic lines on a number of slices in a ROI cropped from the entire volume. Each of the lines intercepts the interfaces between the two phases. Each interception can be considered as an end point of a line

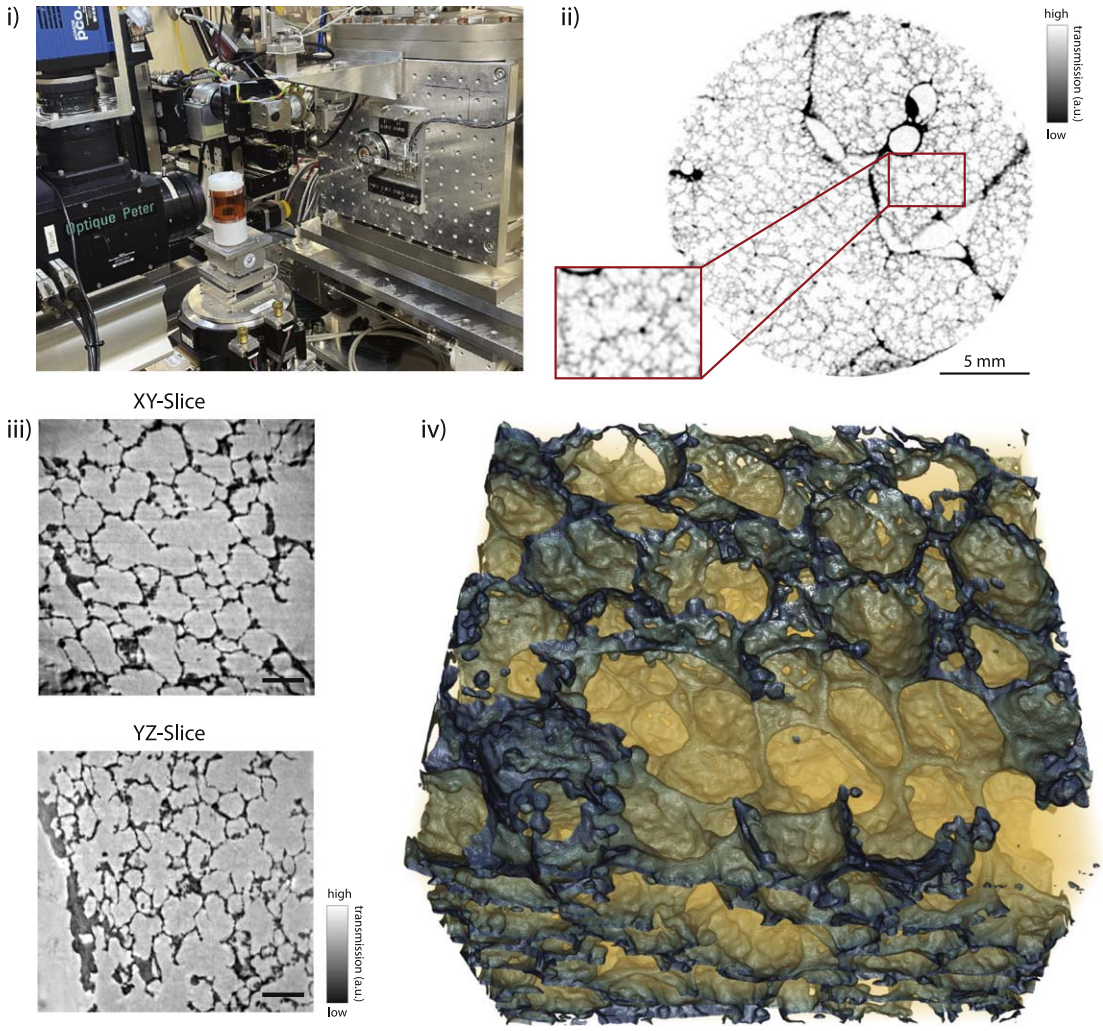

Figure 7. Cryogenically fixed lung tissue. (i) Photograph of the cryo-imaging setup at SR1 with the PCO.edge 5.5 detector (left), sample stage (center) and the beam exit (right). (ii) Slice from an in-house micro-CT scan (Skyscan1272, projections: 700, exp. time: 220 ms, voxel size: 10 μm, energy: 50 keV, scalebar: 5 mm). (iii) Two slices from perpendicular planes from a patient lung with pediatric pulmonary hypertension (scale bar: 0.2 mm). (iv) 3D representation of the segmented tissue (NVIDIA IndeX).

segment. For each of these segments (or chords), the pixel length is calculated using the Bresenham line algorithm (Bresenham 1965) and extracted in tables with chords in phase 0 (paraffin) and phase 1 (tissue). Input data is the logical volume obtained from the segmentation described above (division of the whole reconstruction volume into two phases). Input parameters are the number of line segments to sample, and the minimum length of chords that should be considered. Finally, these chords are displayed in histograms for both phases (LS1-setup, figure 8(i)) see figure 8(ii). The young donor lung shows a smaller amount of short and larger amount of long chord lengths for phase 0, indicating thicker tissue segments in comparison to the old donor. In addition, the young donor biopsy exhibits a larger amount of medium sized chord lengths for phase 1, reflecting the fact that the alveolar spaces are similarly sized and well shaped. Contrarily, the CLD for phase 1 of the old donor lung is much broader, representing a more disordered alveolar network architecture. This interpretation of the quantitative metrics is corroborated by visual inspection, both in the laboratory and the synchrotron data, and also in a rendering of the laboratory dataset (figure S3).

3.6.2. Shape measure analysis

Originally designed as a tool to determine fibre orientation in reconstructed CT datasets of composite materials (Krause *et al* 2010), shape measure analysis recently proved to be a valuable tool in the determination of orientation and geometrical features in biological tissue based on the three-dimensional electron density reflected by the gray values (Reichardt *et al* 2021). In particular, this method is used in this work to determine a fiber-like score which gives indications on the presence of fibrotic human lung tissue. Here, this method is exemplified on a ACD-MPV sample with the rendered results displayed in figure 9. The first step of such a shape measure analysis includes the calculation of a structure tensor which encodes the predominant orientation and

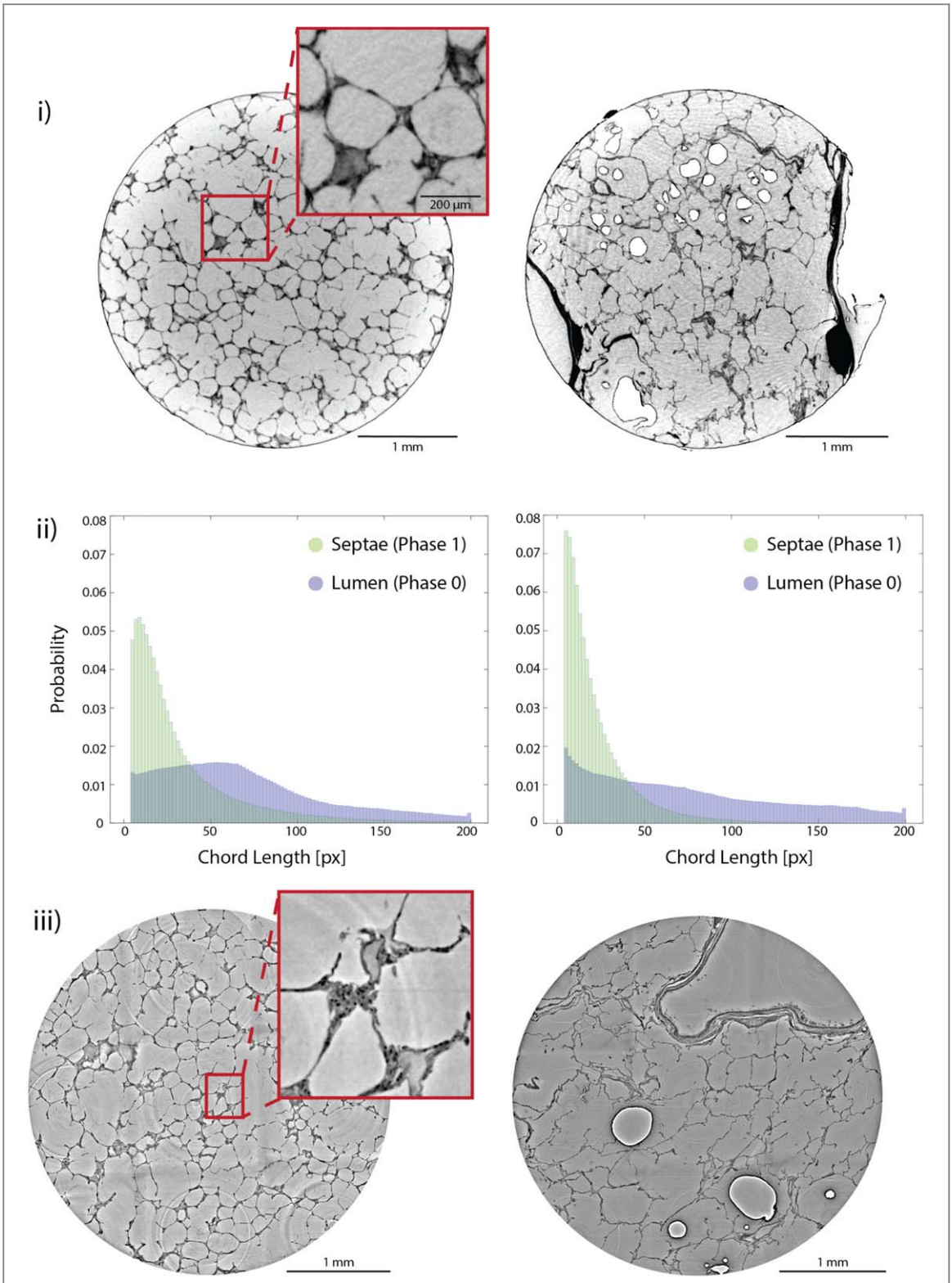

Figure 8. Chord length distribution. (i) Tomographic slices from a young lung donor without any known pathologies (left) and an old lung donor without any pathologies but age-related decay (acquisition settings are tabulated in supplementary table 1: LS1 CLD, scale bar: 1 mm (entire slice), 200 μm (zoom)). (ii) Calculated histograms of the chord length distributions for both donors, quantified for the entire in-house datasets (LS1-setup). Phase 0 represents the alveolar lumen and phase 1 the alveolar septae (left: young donor, right: old donor). (iii) Comparison of the same samples as in (i), recorded with SR1-setup (left: young donor, right: old donor, scale bar: 1 mm, red box width: 350 μm).

degree of anisotropy. The tensor is determined locally for a small test volume and then reported as a 3D map for the entire reconstruction volume. According to (Krause *et al* 2010), the local structure orientation at point **r** is given by the vector

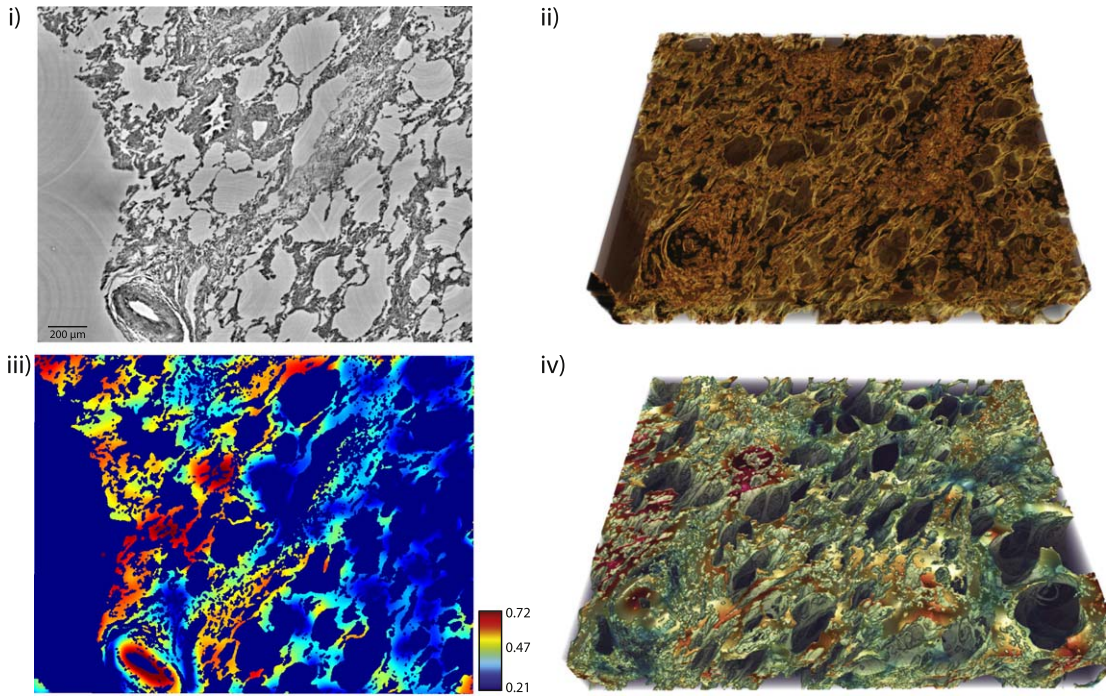

Figure 9. Structure tensor analysis. (i) Cropped region of interest of ACD-MPV sample (SR1-setup). (ii) 3D gray-value based rendering of recorded slice (NVIDIA Index). (iii) Shape measure map applied on the same slice as in (i). For this representation, the shape measures were computed from the tensor of gray value derivatives as described in the main text, and then multiplied by a logical tissue mask, such that the shape measures are only shown for points belonging to tissue. Since fiber-shaped fibrotic tissue is of specific interest, line shaped features were extracted by calculating the first eigenvector of the structure tensor, thus identifying the predominant orientation in a given volume. The color red reflects a high score for linear features and can thus be at least tentatively be associated with areas which are likely to be fibrotic. (iv) Three dimensional display of the line shape measure (again after multiplication with the logical tissue mask), where red indicates a high line shape score. Scale bar: 200 μm.

$$w(\mathbf{r}) = \text{argmin}_{\nu=1}(I(\mathbf{r}+\boldsymbol{\nu}) - I(\mathbf{r}))^2, \tag{1}$$

with $\nu \in \mathrm{R}^3$ and $|\nu| = 1$, where I is a discrete, twice continuously differentiable function describing the gray-value intensity at a point $\boldsymbol{r}$ on the tissue. Due to an ill-posedness of taking gray value derivatives in the computation of gradients for noisy data, the data is first replaced by its smoothed version using a Gaussian filter $I \rightarrow K_\sigma * I$. A second convolution K_ρ is applied to define the length scale over which the orientation is averaged (i.e. essentially the size of the 'test volume'), resulting in the structure tensor J:

$$J = K_\rho * \begin{pmatrix} I_x^2 & I_x I_y & I_x I_z \\ I_y I_x & I_y^2 & I_y I_z \\ I_z I_x & I_z I_y & I_z^2 \end{pmatrix},$$

with I_x representing the partial derivative $\frac{\partial I}{\partial x}$. The minimisation problem (1) can be approximated by its regularised form, which corresponds to the eigenvector of the smallest eigenvalue of J. Thus, the orientation vector $w(\mathbf{r})$ can be obtained for each point $\mathbf{r}$. Contrarily, the direction of the gradient is given by the eigenvector corresponding to the largest eigenvalue of J at any given point (Krause *et al* 2010). In general, the relations between the eigenvalues ($\lambda_1 \geqslant \lambda_2 \geqslant \lambda_3$) reflect the anisotropy and symmetry properties of the local tissue structure, and can be referred to as quantitative shape measures. Namely, the shape measured help to distinguish between local structures exhibiting fiber, planar or spherical symmetry. Here, we chose smoothing values $K_\sigma = 1$ pixel and $K_\rho = 18$ pixels, which seemed reasonably in view of the expected lateral extent of potential fibrotic structures in pixel units at the given magnification. Figure 9(iv) illustrates the results, after multiplication of the shape measure results with a logical mask of the tissue, such that the values are only represented for tissue and not for paraffin. In (iv), the coefficient representing the degree of fiber-like symmetry given by $\frac{\lambda_1}{\lambda_3}$ is displayed according to the colormap.

4. Discussion

Our results indicate an overall surprisingly high image quality even of in-house (laboratory) XPCT scans for the case of FFPE biopsies. This data already allows for segmentation and detailed tissue characterization, including

automated morphometric analysis. As we have shown here, this can be exploited for a wide range of pulmonary pathologies, and can be translated to dedicated and optimized instrumentation which could be operated in clinical setting. By using synchrotron radiation and optimized beamline instrumentation and parameters, the contrast can be further increased to resolve sub μm sized features down to the cellular and sub-cellular level. Furthermore, a wider range of preparations including sample mounting in liquids can be used. Challenging and poorly understood 3D structures such as interbronchial channels can thus be first identified in larger volume overview and subsequently studied in more detail at higher resolution. As a result of having the full 3D structure at hand, the respective physiological functions of airways or vascular networks, and the different pathophysiologic mechanisms can be elucidated or at least underpinned with structural data. At the same time, the synchrotron data can provide ground truth for validation of laboratory data and protocols, important for future standardisation and translation of the method.

Future extension of this work should in particular target sample preparation methods, such as further improvements of PCLS-protocols, developments of novel tissue extraction techniques, or optimized staining agents for certain tissue components (Busse *et al* 2021, Reichmann *et al* 2022). The goal here would be to further improve the overall image contrast, while preserving delicate tissue structures. PCLS protocols and imaging workflows, in particular, must be further optimized for XPCT. It is necessary to avoid sample movement, maintain the native tissue structure at least in terms of the alveolar geometry, and at the same time achieve sufficient contrast between tissue and embedding media. If this is given, XPCT imaging of PCLS could benefit studies of the lung tissue response to viral exposure, as well as the assessment of therapeutics. Furthermore, we can conclude that cryogenic fixation of tissue is a promising approach to study human lung parenchyma in its well preserved original state, ideally with no deformation or damage during tissue extraction and preservation. To this end, cryogenic fixation during sample extraction, known as cryobiopsies (Raghu *et al* 2019), should be considered, as well as adapting more advanced cooling elements such as Peltier cooling, to the different setups used here. Concerning phase retrieval, cryogenically fixed lung tissue can be challenging due to the high contrast between tissue and air, resulting in large phase gradients, which in conventional phase reconstruction such as the CTF-approach result in poor reconstruction quality. Here, further progress by more sophisticated algorithms can be anticipated. Finally, regarding image processing and analysis, the CLD and structure tensor results proved to be highly suitable and further extensions of this explorative study towards standardized workflows and the creation of reference libraries and data for different pathologies could possibly serve automated diagnostic classification.

In summary, this manuscript demonstrates the suitability and versatility of XPCT, being able to image human lung tissue in different embedding media on multiple scales and using a variety of instruments, with high resolutions and large FOV. The technique proves to be well suited to gain further understanding about human lung physiology based on mapping of the three dimensional fine structure of tissue, as well on the highly relevant pathophysiology of a wide range of lung diseases. Quantification of 3D datasets by radiomic tools such as shape measure analysis (figure 9) and chord length distribution (figure 8) allows for an objective assessment of tissue and can help to identify structures not easily detectable, even by the trained eyes of pathologists. In future, this work could be extended towards automatic fibrotic and emphysema quantification. Due to its three-dimensionality and non-destructive nature, virtual histology by XPCT can become a useful extension which can be implemented in a complementary or correlative manner, with respect to existing histological imaging modalities. This would benefit even routine diagnostic assessment in a clinical setting, given further systematic refinement towards this goal.

Acknowledgments

We thank Markus Osterhoff, Michael Sprung, and Fabian Westermeier for excellent support at the GINIX instrument and beamline P10. We also acknowledge assistance in visualization with NVIDIA IndeX (NVIDIA Corporation, USA).

Data availability statement

All data that support the findings of this study are included within the article (and any supplementary information files). Data will be available from 31 January 2023.

Funding

Funded by the Deutsche Forschungsgemeinschaft (DFG, German Research Foundation)—Project-ID 432680300—SFB 1456 and EXC 2067/1-390729940.

Disclosures

The authors declare no conflicts of interest.

Ethical statement

We declare that the human tissue samples have been collected at the following university medical centers:

(1) University Medical Center Göttingen (UMG)
(2) Medical University of Hannover (MHH)
(3) Antwerp Surgical Training, Anatomy and Research Centre (ASTARC)

under the auspices of Prof Dr med. Danny Jonigk (MHH, RWTH), Dr Stijn E Verleden (UZ Leuven, ASTARC) and Priv.-Doz. Dr med. Max Ackermann (UWupp). ID numbers given by the IRB/s (numbered according to institution):

(1) 10/6/20
(2) ID: 9621_BO_K_2021
(3) ID: 0391—Edge 001693—BUN B3002021000073

The research was conducted in accordance with the principles embodied in the Declaration of Helsinki and local statutory requirements and is covered by joint research and ethics proposals. In particular full consent of all donors to participate in the study and for publication of results has been given, and no commercial use or whatsoever exchange of money is involved.

ORCID iDs

Jakob Reichmann https://orcid.org/0000-0002-6597-1831
Jan C Kamp https://orcid.org/0000-0002-5002-409X
Tim Salditt https://orcid.org/0000-0003-4636-0813

References

Ak T P 2021 Bronchus-associated lymphoid tissue (BALT) histology and its role in various pathologies *Updates on Veterinary Anatomy and Physiology* ed D C Rutland and P S El-Gendy (Rijeka: IntechOpen) Section: 9 (https://doi.org/10.5772/intechopen.99366)

Alloo S *et al* 2022 Tomographic phase and attenuation extraction for a sample composed of unknown materials using x-ray propagation-based phase-contrast imaging *Opt. Lett.* **47** 1945–48

Alsafadi H N, Staab-Weijnitz C A, Lehmann M, Lindner M, Peschel B, Königshoff M and Wagner D E 2017 An *ex vivo* model to induce early fibrosis-like changes in human precision-cut lung slices *Am. J. Physiol. Lung Cell. Mol. Physiol.* **312** L896–902

Barbone G *et al* 2022 X-ray multiscale 3D neuroimaging to quantify cellular aging and neurodegeneration postmortem in a model of Alzheimer's disease *Eur. J. Nucl. Med. Mol. Imaging* **49** 4338–57

Bartels M, Hernandez V H, Krenkel M, Moser T and Salditt T 2013 Phase contrast tomography of the mouse cochlea at microfocus x-ray sources *Appl. Phys. Lett.* **103** 083703 Publisher: American Institute of Physics

Bauer C M T, Zavitz C C J, Botelho F M, Lambert K N, Brown E G, Mossman K L, Taylor J D and Stämpfli M R 2010 Treating viral exacerbations of chronic obstructive pulmonary disease: insights from a mouse model of cigarette smoke and H1N1 influenza infection *PLoS One* **5** e13251

Bayat S, Cercos J, Fardin L, Perchiazzi G and Bravin A 2022a Pulmonary vascular biomechanics imaged with synchrotron phase contrast microtomography in live rats *Eur. Respiratory J.* **60** 1741

Bayat S, Fardin L, Cercos-Pita J L, Perchiazzi G and Bravin A 2022b Imaging regional lung structure and function in small animals using synchrotron radiation phase-contrast and K-edge subtraction computed tomography *Frontiers Physiol.* **13** 825433

Bayat S, Porra L, Suortti P and Thomlinson W 2020 Functional lung imaging with synchrotron radiation: methods and preclinical applications *Physica Medica: Eur. J. Med. Phys.s* **79** 22–35 Publisher: Elsevier

Bishop N B, Stankiewicz P and Steinhorn R H 2011 Alveolar capillary dysplasia *Am. J. Respiratory Crit. Care Med.* **184** 172–9

Borisova E, Lovric G, Miettinen A, Fardin L, Bayat S, Larsson A, Stampanoni M, Schittny J C and Schlepütz C M 2021 Micrometer-resolution x-ray tomographic full-volume reconstruction of an intact post-mortem juvenile rat lung *Histochemistry Cell Biol.* **155** 215–26

Bresenham J E 1965 Algorithm for computer control of a digital plotter *IBM Syst. J.* **4** 25–30 Conference Name: IBM Systems Journal

Busse M, Marciniszyn J P, Ferstl S, Kimm M A, Pfeiffer F and Gulder T 2021 3D-Non-destructive imaging through heavy-metal eosin salt contrast agents *Chem.—A Eur. J.* **27** 4561–6

Campbell J D *et al* 2012 A gene expression signature of emphysema-related lung destruction and its reversal by the tripeptide GHK *Genome Med.* **4** 67

Cetti E J, Moore A J and Geddes D M 2006 Collateral ventilation *Thorax* **61** 371–3

Chung S-Y, Sikora P, Rucińska T, Stephan D and Abd Elrahman M 2020 Comparison of the pore size distributions of concretes with different air-entraining admixture dosages using 2D and 3D imaging approaches *Mater. Charact.* **162** 110182
Cloetens P, Ludwig W, Baruchel J, Van Dyck D, Van Landuyt J, Guigay J P and Schlenker M 1999 Holotomography: quantitative phase tomography with micrometer resolution using hard synchrotron radiation x rays *Appl. Phys. Lett.* **75** 2912–4
Cooper P R and Panettieri R A 2008 Steroids completely reverse albuterol-induced β2-adrenergic receptor tolerance in human small airways *J. Allergy Clin Immunol.y* **122** 734–40
Crowley G, Kwon S, Caraher E J, Haider S H, Lam R, Batra P, Melles D, Liu M and Nolan A 2019 Quantitative lung morphology: semi-automated measurement of mean linear intercept *BMC Pulmonary Med.* **19** 206
Dejea H, Garcia-Canadilla P, Cook A C, Guasch E, Zamora M, Crispi F, Stampanoni M, Bijnens B and Bonnin A 2019 Comprehensive analysis of animal models of cardiovascular disease using multiscale x-ray phase contrast tomography *Sci. Rep.* **9** 6996
Deutsch G H *et al* 2007 Diffuse lung disease in young children *Am. J. Respiratory Crit. Care Med.* **176** 1120–8
Ding Y *et al* 2019 Computational 3D histological phenotyping of whole zebrafish by x-ray histotomography *eLife* **8** e44898 Publisher: eLife Sciences Publications, Ltd
Donovan C, Seow H J, Bourke J E and Vlahos R 2016 Influenza a virus infection and cigarette smoke impair bronchodilator responsiveness to beta-adrenoceptor agonists in mouse lung *Clin. Sci. (London, England: 1979)* **130** 829–37
Eckermann M, Töpperwien M, Robisch A-L, van der Meer F, Stadelmann C and Salditt T 2019 Phase-contrast x-ray tomography of neuronal tissue at laboratory sources with submicron resolution *X-Ray Nanoimaging: Instruments and Methods IV* ed B Lai and A Somogyi (San Diego, United States: SPIE) 26
Eckermann M *et al* 2020 3D virtual pathohistology of lung tissue from Covid-19 patients based on phase contrast x-ray tomography *eLife* **9** e60408 Publisher: eLife Sciences Publications, Ltd
Eggl E, Schleede S, Bech M, Achterhold K, Loewen R, Ruth R D and Pfeiffer F 2015 X-ray phase-contrast tomography with a compact laser-driven synchrotron source *Proc. Natl. Acad. Sci.* **112** 5567–72 Publisher: Proceedings of the National Academy of Sciences
Frohn J, Pinkert-Leetsch D, Missbach-Güntner J, Reichardt M, Osterhoff M, Alves F and Salditt T 2020 3D virtual histology of human pancreatic tissue by multiscale phase-contrast x-ray tomography *J. Synchrotron. Radiat.* **27** 1707–19
Gerckens M, Alsafadi H N, Wagner D E, Lindner M, Burgstaller G and Königshoff M 2019 Generation of human 3D lung tissue cultures (3D-LTCs) for disease modeling *J. Visualized Exp* **144** e58437
Hemberg O, Otendal M and Hertz H M 2003 Liquid-metal-jet anode electron-impact x-ray source *Appl. Phys. Lett.* **83** 1483–5 Publisher: American Institute of Physics
Huhn S, Lohse L M, Lucht J, Salditt T *et al* 2022 Fast algorithms for nonlinear and constrained phase retrieval in near-field X-ray holography based on Tikhonov regularization *Optics Express* **30** 32871–32886
Kennedy J L *et al* 2018 Effects of rhinovirus 39 infection on airway hyperresponsiveness to carbachol in human airways precision cut lung slices *J. Allergy and Clin. Immunol.* **141** 1887–90
Khimchenko A, Deyhle H, Schulz G, Schweighauser G, Hench J, Chicherova N, Bikis C, Hieber S E and Müller B 2016 Extending two-dimensional histology into the third dimension through conventional micro computed tomography *NeuroImage* **139** 26–36
Khimchenko A *et al* 2018 Hard x-ray nanoholotomography: large-scale, label-free, 3D neuroimaging beyond optical limit *Adv. Sci.* **5** 1700694
Knudsen L, Weibel E R, Gundersen H J G, Weinstein F V and Ochs M 2010 Assessment of air space size characteristics by intercept (chord) measurement: an accurate and efficient stereological approach *J. Appl. Physiol.* **108** 412–21 Publisher: American Physiological Society
Krause M, Hausherr J M, Burgeth B, Herrmann C and Krenkel W 2010 Determination of the fibre orientation in composites using the structure tensor and local x-ray transform *J. Mater. Sci.* **45** 888–96
Krenkel M, Markus A, Bartels M, Dullin C, Alves F and Salditt T 2015 Phase-contrast zoom tomography reveals precise locations of macrophages in mouse lungs *Sci. Rep.* **5** 9973
Latypov M I, Kühbach M, Beyerlein I J, Stinville J-C, Toth L S, Pollock T M and Kalidindi S R 2018 Application of chord length distributions and principal component analysis for quantification and representation of diverse polycrystalline microstructures *Mater. Charact.* **145** 671–85
Leong A F T, Buckley G A, Paganin D M, Hooper S B, Wallace M J and Kitchen M J 2014 Real-time measurement of alveolar size and population using phase contrast x-ray imaging *Biomed. Opt. Express* **5** 4024–38 Publisher: Optica Publishing Group
Liu G, Betts C, Cunoosamy D M, Åberg P M, Hornberg J J, Sivars K B and Cohen T S 2019 Use of precision cut lung slices as a translational model for the study of lung biology *Respiratory Res.* **20** 162
Lohse L, Robisch A-L, Töpperwien M, Maretzke S, Krenkel M, Hagemann J and Salditt T 2020 A phase-retrieval toolbox for x-ray holography and tomography *J. Synchrotron Radiat.* **27** 852–859
MacIver M R and Pawlik M 2017 Analysis of *in situ* microscopy images of flocculated sediment volumes *Chem. Eng. Technol.* **40** 2305–13
Maclver R M 2022 Chord length distribution from binary 2D images, https://mathworks.com/matlabcentral/fileexchange/64909-chord-length-distribution-from-binary-2d-images
Maes A *et al* 2022 Cryogenic contrast-enhanced microCT enables nondestructive 3D quantitative histopathology of soft biological tissues *Nat. Commun.* **13** 6207
Martin C, Uhlig S and Ullrich V 1996 Videomicroscopy of methacholine-induced contraction of individual airways in precision-cut lung slices *Eur. Respiratory J.* **9** 2479–87 Publisher: European Respiratory Society Section: Original Articles
Martin H B 1966 Respiratory bronchioles as the pathway for collateral ventilation *J. Appl. Physiol.* **21** 1443–7
Massimi L, Suaris T, Hagen C K, Endrizzi M, Munro P R, Havariyoun G, Hawker P M, Smit B, Astolfo A and Larkin O J 2021 Detection of involved margins in breast specimens with x-ray phase-contrast computed tomography *Sci. Rep.* **11** 1–9 Publisher: Nature Publishing Group
Massimi L *et al* 2019 Exploring Alzheimer's disease mouse brain through x-ray phase contrast tomography: from the cell to the organ *NeuroImage* **184** 490–5
Melly L, Sebire N J, Malone M and Nicholson A G 2008 Capillary apposition and density in the diagnosis of alveolar capillary dysplasia *Histopathology* **53** 450–7
Mercer P F *et al* 2016 Exploration of a potent PI3 kinase/mTOR inhibitor as a novel anti-fibrotic agent in IPF *Thorax* **71** 701–11
Meyerholz D K, Suarez C J, Dintzis S M and Frevert C W 2018 Respiratory System *Comparative Anatomy and Histology* (New York: Elsevier) 147–62
Morgan K S *et al* 2020 Methods for dynamic synchrotron x-ray respiratory imaging in live animals *J. Synchrotron Radiat.* **27** 164–75
Münch B, Trtik P, Marone F and Stampanoni M 2009 Stripe and ring artifact removal with combined wavelet—Fourier filtering *Opt. Express* **17** 8567–8591

Norvik C et al 2020 Synchrotron-based phase-contrast micro-CT as a tool for understanding pulmonary vascular pathobiology and the 3D microanatomy of alveolar capillary dysplasia *Am. J. Physiol.-Lung Cell. Mol. Physiol.* **318** L65–75 Publisher: American Physiological Society

O'Connell D W et al 2022 Accurate measures of changes in regional lung air volumes from chest x-rays of small animals *Phys. Med. Biol.* **67** 205002

Paganin D and Nugent K A 1998 Noninterferometric phase imaging with partially coherent light *Phys. Rev. Lett.* **80** 2586–9 Publisher: American Physical Society

Palermo F et al 2022 Multilevel x-ray imaging approach to assess the sequential evolution of multi-organ damage in multiple sclerosis *Commun. Phys.* **5** 290

Parsons D W, Morgan K, Donnelley M, Fouras A, Crosbie J, Williams I, Boucher R C, Uesugi K, Yagi N and Siu K K W 2008 High-resolution visualization of airspace structures in intact mice via synchrotron phase-contrast x-ray imaging (PCXI) *J. Anatomy* **213** 217–27

Raghu G, Lederer D J and Rabe K F 2019 Cryobiopsy for interstitial lung disease: the heat is on *Am. J. Respiratory Crit. Care Med.* **199** 1183–4

Reichardt M et al 2021 3D virtual histopathology of cardiac tissue from Covid-19 patients based on phase-contrast x-ray tomography *eLife* **10** e71359 Publisher: eLife Sciences Publications, Ltd

Reichmann J, Ruhwedel T, Möbius W and Salditt T 2022 Neodymium acetate as a contrast agent for x-ray phase-contrast tomography *Developments in X-Ray Tomography XIV* Vol 12242 (SPIE) 8–23

Ricke-Hoch M et al 2021 Impaired immune response mediated by prostaglandin E2 promotes severe COVID-19 disease *PLoS One* **16** e0255335 Publisher: Public Library of Science

Ritchie H, Spooner F and Roser M 2018 Causes of death *Our World in Data* **90** 108–109

Saccomano M, Albers J, Tromba G, Dobrivojević Radmilović M, Gajović S, Alves F and Dullin C 2018 Synchrotron inline phase contrast μCT enables detailed virtual histology of embedded soft-tissue samples with and without staining *J. Synchrotron Radiat.* **25** 1153–61 Publisher: International Union of Crystallography

Salditt T, Osterhoff M, Krenkel M, Wilke R N, Priebe M, Bartels M, Kalbfleisch S and Sprung M 2015 Compound focusing mirror and X-ray waveguide optics for coherent imaging and nano-diffraction *J. Synchrotron Radiat.* **22** 867–78 Publisher: International Union of Crystallography

Sato J, Chida K, Suda T, Sato A and Nakamura H 2000 Migratory patterns of thoracic duct lymphocytes into bronchus-associated lymphoid tissue of immunized rats *Lung* **178** 295–308

Schindelin J et al 2012 Fiji: an open-source platform for biological-image analysis *Nat. Methods* **9** 676–82 Publisher: Nature Publishing Group

Schneider E, Robertson B, Kuhn A, Lux C and Nienhaus M 2021 NVIDIA index accelerated computing for visualizing Cholla's galactic winds *Parallel Comput.* **107** 102809

Shaker K, Häggmark I, Reichmann J, Arsenian-Henriksson M and Hertz H M 2021 Phase-contrast x-ray tomography resolves the terminal bronchioles in free-breathing mice *Commun. Phys.* **4** 259

Sminia T, van der Brugge-Gamelkoorn G and van der Ende M B 1990 Bronchus-associated lymphoid tissue, rat, normal structure *Monographs on pathology of laboratory animals* ed T C Jones et al (Berlin, Heidelberg: Springer) pp 299–307

Stahr C S et al 2016 Quantification of heterogeneity in lung disease with image-based pulmonary function testing *Sci. Rep.* **6** 29438 Publisher: Nature Publishing Group

Temann A, Golovina T, Neuhaus V, Thompson C, Chichester J A, Braun A and Yusibov V 2017 Evaluation of inflammatory and immune responses in long-term cultured human precision-cut lung slices *Human Vaccines & Immunotherapeutics* **13** 351–8

Terry P B and Traystman R J 2016 The clinical significance of collateral ventilation *Ann. Am. Thoracic Soc.* **13** 2251–7

Töpperwien M 2018 *3d Virtual Histology of Neuronal Tissue by Propagation-based X-ray Phase-contrast Tomography* (Göttingen: Göttingen University Press) Göttingen Series in x-ray Physics

Töpperwien M, Krenkel M, Müller K and Salditt T 2016 Phase-contrast tomography of neuronal tissues: from laboratory- to high resolution synchrotron CT *Developments in X-Ray Tomography X* Vol. 9967 (SPIE) 64–79

Töpperwien M, van der Meer F, Stadelmann C and Salditt T 2018 Three-dimensional virtual histology of human cerebellum by x-ray phase-contrast tomography *PNAS* **115** 6940–5

Torgerson D G et al 2011 Meta-analysis of genome-wide association studies of asthma in ethnically diverse North American populations *Nat. Genet.* **43** 887–92

Tschernig T and Pabst R 2000 Bronchus-associated lymphoid tissue (BALT) is not present in the normal adult lung but in different diseases *Pathobiol.y: Jo. Immunopathol., Mol. Cell. Biol.* **68** 1–8

Turner D M, Niezgoda S R and Kalidindi S R 2016 Efficient computation of the angularly resolved chord length distributions and lineal path functions in large microstructure datasets *Modell. Simul. Mater. Sci. Eng.* **24** 075002 Publisher: IOP Publishing

van Essen H F, Verdaasdonk M A M, Elshof S M, de Weger R A and van Diest P J 2010 Alcohol based tissue fixation as an alternative for formaldehyde: influence on immunohistochemistry *J. Clin. Pathol.* **63** 1090–4 Place: England

Vasilescu D M et al 2017 Nondestructive cryomicro-CT imaging enables structural and molecular analysis of human lung tissue *J. Appl. Physiol.* **122** 161–9

Verleden S E et al 2022 From macroscopy to ultrastructure: an integrative approach to pulmonary pathology *Frontiers Med.* **9** 859337

Westöö C et al 2021 Distinct types of plexiform lesions identified by synchrotron-based phase-contrast micro-CT *Am. J. Physiol.-Lung Cell. Mol. Physiol.* Publisher: American Physiological Society Rockville, MD **321** L17–L28

Witte Y D, Boone M, Vlassenbroeck J, Dierick M and Hoorebeke L V 2009 Bronnikov-aided correction for x-ray computed tomography *J. Opt. Soc. Am.* **26** 890–4 Publisher: Optica Publishing GroupA